Contents lists available at ScienceDirect

Nuclear Inst. and Methods in Physics Research, B

On quantitative off-axis Scanning Transmission Ion Microscopy (STIM)

Harry J. Whitlow [*]

Norwegian Micro- and NanoFabrication Facility Laboratory, Department of Physics, University of Oslo, Postboks 1048 Blindern, Oslo, N-0316, Norway
Tandem Laboratory, Uppsala University, P.O. Box 529, Uppsala, SE-751 21, Sweden

A B S T R A C T

Spurred by a need to determine major (C, H, N and O) contents in biological tissue sections, a formalism for quantitative off-axis Scanning Transmission Ion Microscopy (OA-STIM) has been established. This can be used with, or without, simultaneous Elastic Backscattering Spectroscopy (EBS) to provide quantitative major element composition and thickness information. As part of the work, an empirical predictor with one free parameter for the proton–proton differential scattering cross section was implemented. The predictor values were in extremely close agreement with high accuracy literature data. For 2 MeV p–^{12}C elastic scattering at forward angles ≤45° an interpolation procedure was used to determine the relative deviations from the Rutherford cross sections were determined to be ≤6.4%. The interpolation was based on a Coulomb field, angular momentum quantum number and nuclear structure dependent nuclear penetration factor. Finally, the quantitative combination of simultaneous OA-STIM and EBS data is discussed.

1. Introduction

Off-axis Scattering Transmission Ion Microscopy (OA-STIM) is an MeV-ion microprobe imaging method [1]. This method employs an energy detector placed at a forward angle ($\theta < 90°$) to detect scattered ions and recoil atoms for a thin sample. The forward-scattering implies hydrogen can be measured using OA-STIM. This is useful because Particle Induced X-ray Emission (PIXE) and Elastic Backscattering Spectrometry (EBS) are both blind to hydrogen. Direct-STIM methods measure the energy-loss of ions that traverse the sample, providing structural but no elemental information. The absence of scattering in Direct-STIM implies every ion can be detected which allows extremely finely focused low-current ions beams to be used for extremely high spatial resolution (20–50 nm) structural imaging e.g. Refs. [2,3]. Coincidence Elastic Recoil Detection Analysis (coincidence-ERDA) is a conceptually similar method to OA-STIM where two detectors are used to detect scattered and recoil atoms from a single collision in coincidence [4]. Although coincidence-ERDA has a high selectivity, useful information from forward-scattering of ions from other elements and some depth information can be lost. Proton Elastic Scattering Analysis (PESA) is also conceptually similar to OA-STIM and used for broad-beam analysis of hydrogen in aerosols on uniform hydrogen-free support films [5–7].

Hydrogen, is an important element. In biological materials it is a major element and as such constitutes ~9.5 mass % of the human body [8,9]. Hydrogen is also a major element in many polymers (e.g. for polyethylene where H makes up 66.6 at. %). It is also present as hydrate in many minerals and appreciable amounts can be detected even in anhydrous minerals (garnet, olivine and pyroxenes) [10]. Hydrogen transport plays a key part in corrosion suppression, fuel-cell, photovoltaic and battery technologies.

The present work was driven by the need to measure the thickness and content of the major elements (H, C, N, O) in the matrix of biological tissue sections as a prerequisite for accurate PIXE determination of the heavy lesser and trace-element contents [11]. The major element composition determines the electron density which in turn governs the stopping force ($-dE/dx$) as well as the X-ray absorption which are key parameters in quantitative PIXE analysis. OA-STIM combined with EBS is well-suited for measuring the major element composition and thickness of biological tissue sections because the former can provide H-content and sample thickness information and the latter gives the content of other major elements. Although for thin biological samples the EBS and OA-STIM yields per pixel are small, the method can be used to measure aggregate elemental compositions in areas corresponding to different types of tissue which span many pixels [11].

2. OA-STIM formalism

The formalism for quantitative OA-STIM analysis is developed in three parts. The first deals with the relation between energy-loss and

---

* Corresponding author at: Norwegian Micro- and NanoFabrication Facility Laboratory, Department of Physics, University of Oslo, Postboks 1048 Blindern, Oslo, N-0316, Norway.
E-mail address: h.j.whitlow@fys.uio.no.
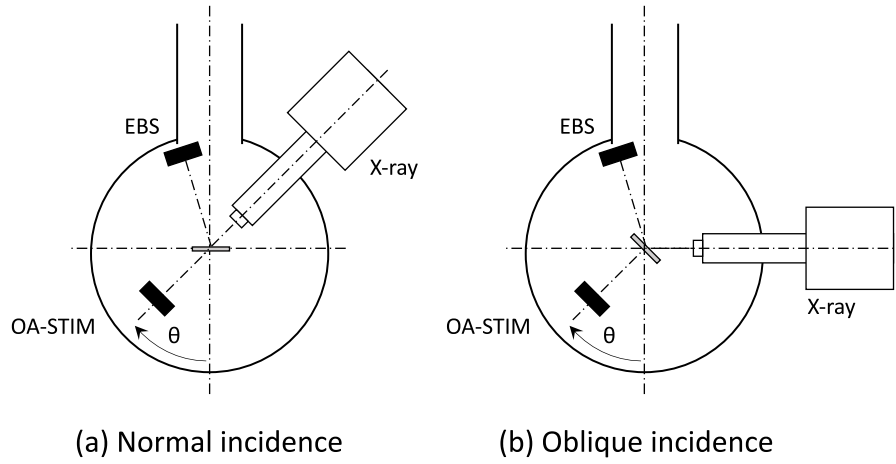
(a) Normal incidence   (b) Oblique incidence

Fig. 1. Detector configurations for (a) normal incidence, (b) oblique incidence to the sample surface.

thickness. The second addresses low-energy proton – proton and proton – ^{12}C elastic scattering cross sections. The final part concerns establishing a quantitative relation between the OA-STIM and EBS data.

2.1. Basic equations

The kinematic factors K for scattering and recoils Λ are,

$$K = \left[\frac{\left(M_2^2 - M_1^2 \sin^2 \theta_l\right)^{\frac{1}{2}} + M_1 \cos \theta_l}{M_1 + M_2} \right]^2 \quad (1)$$

and,

$$\Lambda = \frac{4 M_1 M_2}{\left(M_1 + M_2\right)^2} \cos^2 \phi_l. \quad (2)$$

The atomic numbers are Z_1 and Z_2 and masses M_1 and M_2 where the subscripts 1 and 2 refer to the projectile and target atoms, respectively. Subscript l denotes quantities in the laboratory reference frame. For the case of forward scattered particles with $M_1 = M_2$ as in p–p scattering, at an angle $\theta_l = \phi_l$ then $M_1 = M_2$ and $K = \Lambda$.

The Rutherford differential scattering cross section from [12] can be expressed in SI units as,

$$\left(\frac{d\sigma_R}{d\Omega}\right)_c = \left(\frac{Z_1 Z_2 e^2}{16 \pi \varepsilon_0 E_c \sin^2\left(\theta_c/2\right)}\right)^2. \quad (3)$$

e is the elementary charge and ε_0 is the permittivity of free space. Subscript c denotes quantities in the centre of mass reference frame. $\gamma = M_1/M_2$, $E_c = E_l/(1+\gamma)$ and $\theta_c = \theta_l \sin^{-1}\left(\gamma \sin \theta_l\right)$ for $\gamma \leq 1$. Invoking conservation of particles in elastic scattering [13];

$$\left(\frac{d\sigma_R}{d\Omega}\right)_l = \frac{\left(1 + 2\gamma \cos \theta_c + \gamma^2\right)^{\frac{3}{2}}}{1 + \gamma \cos \theta_c} \left(\frac{d\sigma_R}{d\Omega}\right)_c. \quad (4)$$

A more direct form proposed by Ziegler and Lever [14] gives;

$$\left(\frac{d\sigma_R}{d\Omega}\right)_l = \left(\frac{Z_1 Z_2 e^2}{\pi \varepsilon_0 E_l}\right)^2 \sin^{-4} \theta_l \frac{\left[\left(1 - \gamma^2 \sin^2 \theta_l\right)^{\frac{1}{2}} - \cos \theta_l\right]^2}{\left(1 - \gamma^2 \sin^2 \theta_l\right)^{\frac{1}{2}}}. \quad (5)$$

Eqs. (3) and (4) give better computational accuracy than Eq. (5) at large θ_l.

3. Energy-loss and thickness

Two basic configurations have been used at different laboratories for OA-STIM. These are schematically shown in Fig. 1. The formalism
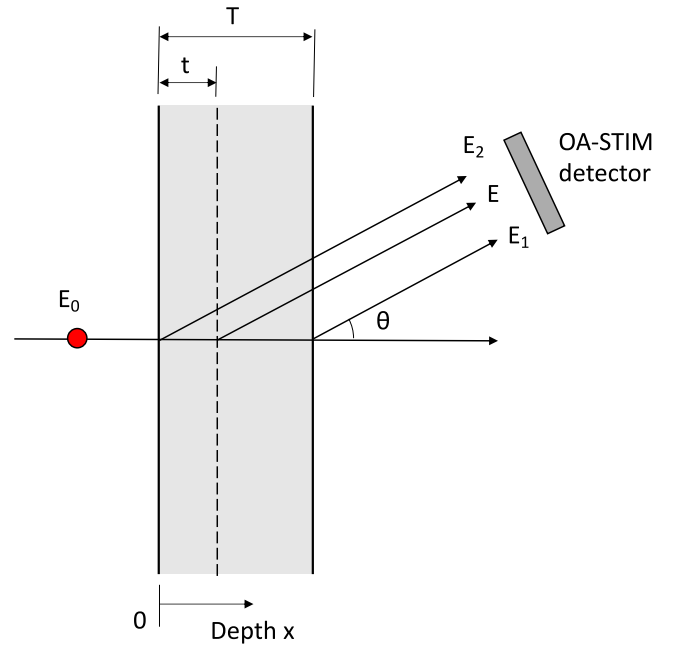

Fig. 2. Geometric configuration for OA-STIM.

for the normal incidence configuration is considered here as it is more straightforward. For moderate oblique angles, the extension from the normal incidence case requires only the introduction of some trigonometric factors to account for the longer path lengths along the inward and outward paths. Fig. 2 presents the geometric configuration for normal incidence OA-STIM. For the parameters defined in this figure, the energy for scattering and recoiling of ions into a detector at angle θ from depth t is,

$$E = K E_0 - K N \int_0^t dx \, \epsilon_{in}(x) - N \int_t^T dx \frac{\epsilon_{out}(x)}{\cos \theta}. \quad (6)$$

$\epsilon_{in}(x)$ and $\epsilon_{out}(x)$ are the stopping cross sections along the inward path (before scattering) and outward path (after scattering), respectively. N is the number of atoms per unit volume. The integrals emphasise that for the transmission geometry the energy losses take place along the entire sample thickness. This makes the formalism more intricate than glancing-angle stopper-foil [15], ToF-E ERDA [16] and RBS [12,15].

E_1 and E_2, (Fig. 2) correspond to the energies for scattering from the front and rear surfaces of the sample. They can be found by putting
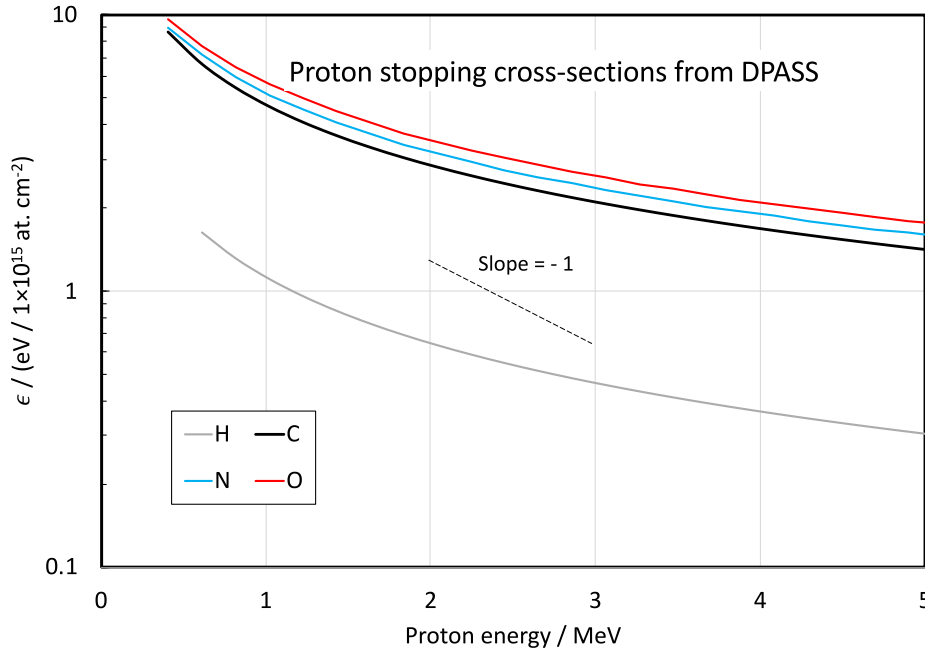
Fig. 3. Stopping cross sections for the major elements in biological tissue from DPASS [17,18].

$t = T$ and $t = 0$, respectively into Eq. (6),

$$E_1 = KE_0 - NK \int_0^T dx\epsilon_{in}(x) \tag{7}$$

$$E_2 = KE_0 - N \int_0^T dx \frac{\epsilon_{out}(x)}{\cos\theta}. \tag{8}$$

Fig. 3 presents the energy dependence of the stopping cross-sections ϵ for protons in H, C, N and O from the ab inito DPASS code [17,18]. Bragg's rule [12,15,18] can be used to obtain ϵ values for mixtures of target elements. Deviations from Bragg's rule may occur [19]. A review [20] suggests this is the order of a few % for hydrocarbons. It should be borne in mind the deviations from experiment will depend on the stopping force predictor used. Fig. 3, which spans the energy range relevant for OA-STIM measurements, shows (i) that ϵ increases with decreasing energy and (ii) that the rate of increase of ϵ increases with decreasing energy. This together with Eqs. (7) and (8) and also that both K and $\cos\theta$ are < 1 implies that $E_1 > E_2$ for all T. This gives an important result that *ions scattered from the rear face of the sample have the highest energy and those scattered from the front face have the lowest energy.*

Taking the energy difference between Eq. (6) and an infinitely thin sample $T \to 0$ so that $E = KE_0$ gives,

$$\Delta E = KE_0 - E$$
$$= N \left[K \int_0^t dx\epsilon_{in}(x) + \int_t^T dx \frac{\epsilon_{out}(x)}{\cos\theta} \right] \tag{9}$$
$$\simeq Nt [\bar{\epsilon}].$$

where, $[\bar{\epsilon}]$ is a mean stopping cross section factor. Then for a sample that is sufficiently thin so that ϵ_{in} and ϵ_{out} can be taken to be constants,

$$\Delta E = N \left[tK\epsilon_{in} + (T - t) \frac{\epsilon_{out}}{\cos\theta} \right]. \tag{10}$$

From the ratio of the partial derivatives $\partial\Delta E/\partial t$ and $\partial\Delta E/\partial T$ of Eq. (10), after some manipulation, the ratio of the variances of the measured depth δt^2 to sample thickness δT^2 is $1/(a-1)^2$. Where $a = K(\epsilon_{in}/\epsilon_{out})\cos\theta \sim 0.5$ giving $\delta t^2/\delta T^2 \sim 4$. *Thus variations in the sample thickness can have a major influence on the shape of the OA-STIM energy spectrum.* This is significant because sample thickness variations are commonly encountered in OA-STIM analysis. These can arise

from dehydration, sample preparation as well as voids and multiphase regions. Examples include papers, textile structures, crystal grains, particulate matter, different tissue regions in biological samples etc. Energy broadening will be contributed to by the thickness variations (discussed above), energy loss straggling and path length differences from multiple scattering across the entire ion trajectory through the sample. These contributions will be exuberated for increasingly oblique ion trajectories. In this case the influence of thickness variations is a minimum because the ions traverse the sample in a direction normal to the surface. For determination of the local sample thickness where thickness variations are present, is then preferable to measure the energy shift of the high energy edge ΔE_1 which corresponds to ions scattered from the rear surface of the sample (Eq. (7)). This procedure is illustrated in Ref. [11] where different regions of biological tissue sections gave rise to different OA-STIM spectra. For normal incidence, path length differences due to multiple scattering are negligible. This may become problematic for extreme glancing incidence. The half-angle at half-width of the angular distribution for 2 MeV protons is ~6 mr for 10 µm for mylar [21] which has similar composition to dry biological tissue and many polymers. Moreover, the shorter traverse for normal incidence implies the influence of the energy dependence of the stopping cross sections is smaller which can simplify the analysis by allowing the surface energy approximation to be used to determine the stopping cross sections.

Furthermore, in some cases the sample thickness may be sufficiently large so that the integrals of the energy loss (Eq. (6)) need to be taken into account. In these cases, determination of a full elemental depth profile from OA-STIM will require fitting a simulated spectrum where the energy dependence of energy loss, thickness and scattering cross section variations are fully taken into account. Where elemental composition variations along the probing ions trajectory are important, quantitative element depth profiles, including H, could determined using a iterative procedure. As a first approximation the elemental profiles derived from EBS with an appropriate zero-order assumption as to the hydrogen concentration distribution is made. These concentration profiles are used to refine the H-concentration profile from the OA-STIM data. In subsequent iteration(s), the concentration profiles from previous iterations(s) are used to refine the stopping cross sections values which are then used to determine more precise elemental concentration profiles for all elements from the EBS and OA-STIM spectra.
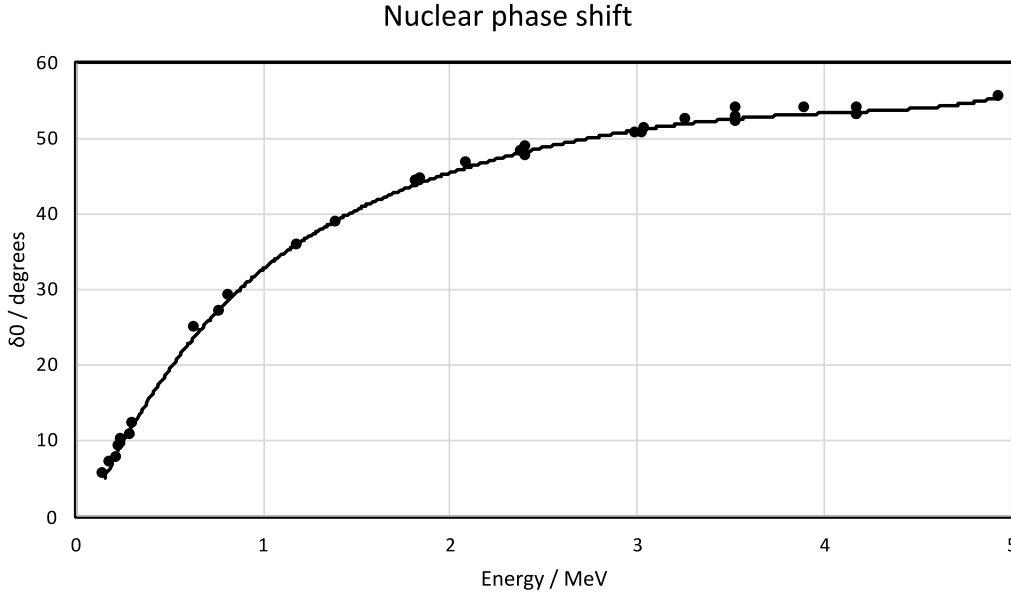
Nuclear phase shift

Fig. 4. Empirical fit for the energy dependence of the nuclear s-wave phase shift using data from Refs. [22–24] collected by Evans [25].

4. Elastic scattering cross section for OA-STIM

4.1. Proton–proton scattering

Historically, p–p scattering has been studied intensively from the 1940s to 60s [22]. Today, low-energy p–p scattering is one of the best quantitatively understood nuclear interactions. It is fundamentally important because it represents a pure interaction between two identical nucleons. Scattering from both the Coulomb and nuclear forces must be considered in p–p scattering. Furthermore, protons are fermions with spin quantum number $s = \pm 1/2$, The situation is then similar to, but not identical with, the Mott scattering of electrons [26] which governs the electron cascades that limit the resolution in electron microscopy, electron beam lithography and proton beam writing. The important difference between the electron and proton case being that for p–p scattering both the Coulomb and the nuclear forces contribute significantly to scattering and interference. Jacksson and Blatt [22] derived an expression for the differential scattering cross-section in the centre of mass reference frame. From this and standard texts, the p–p elastic cross section can be expressed in SI units as [25,27];

$$\left(\frac{d\sigma}{d\Omega}\right)_c = \left(\frac{e^2}{8\pi\varepsilon_0 E_l}\right)^2 \sum_{i=0}^{i=6} a_i, \tag{11}$$

where;

$$a_0 = \frac{1}{\sin^4\left(\theta_c/2\right)}, \tag{12}$$

$$a_1 = \frac{1}{\cos^4\left(\theta_c/2\right)}, \tag{13}$$

$$a_2 = -\frac{\cos\left[\eta \ln \tan^2\left(\theta_c/2\right)\right]}{\sin^2\left(\theta_c/2\right)\cos^2\left(\theta_c/2\right)}, \tag{14}$$

$$a_3 = -\frac{2}{\eta}\sin\delta_0\left\{\frac{\cos\left[\delta_0 + \ln\sin^2\left(\theta_c/2\right)\right]}{\sin^2\left(\theta_c/2\right)} + \frac{\cos\left[\delta_0 + \ln\cos^2\left(\theta_c/2\right)\right]}{\cos^2\left(\theta_c/2\right)}\right\}, \tag{15}$$

$$a_4 = \frac{4}{\eta^2}\sin^2\delta_0, \tag{16}$$

and;

$$a_5 = a_6 = 0. \tag{17}$$

The subscript c denotes quantities in the centre of mass frame. $\eta = \alpha/\beta$ were $\alpha = e^2/\left(4\pi\varepsilon_0\hbar c\right)$, is the fine structure constant and $\beta = v_c/c$. v_c is the velocity in the centre of mass frame. The term a_0 (Eq. (12)) originates from protons scattered by the Coulomb potential at an angle θ_l, a_1, (Eq. (13)) corresponds to protons recoiled at the same θ_l, a_2 is the Mott scattering term [26] (Eq. (14)) [28], a_3 (Eq. (15)) is from interference between nuclear s-wave and Coulomb-scattered protons [25], a_4, (Eq. (16)) corresponds to scattering by the nuclear s-wave [22,27]. In Eqs. (11) – (16), the only free-parameter is the nuclear s-wave phase shift δ_0, which enters into Eqs. (15) and (16). δ_0 was approximated from the collected data of Refs. [22–24] plotted by Evans (Fig. 5.3 in Ref. [25]), by fitting to a polynomial as shown in Fig. 4.

$$\delta_0 = \sum_{j=0}^{j=5} h_j E_l^j; \tag{18}$$

were, $h_0 = -3.10770949$, $h_1 = 58.2641333$, $h_2 = -30.3242220$, $h_3 = 9.32643682$, $h_4 = -1.53519384$, $h_5 = 0.102188800$.

An alternative formula that smooths away the high energy kink in the data has the form $\tan\delta = A - B\exp{-CE}$, with $A = 54.70805971$, $B = 57.22258557$ and $C = 0.91198208$. Both formulas are likely to be unreliable if extrapolated outside of the energy range spanned by the experimental data.

The nuclear p-wave and vacuum polarisation terms a_5 and a_6 (Eq. (17)) are small and uncertain over the range of interest for OA-STIM [28–30]. These were neglected since the goal was to develop a predictor code for the p–p scattering cross section in OA-STIM.

The contributions a_0–a_4 to the total differential scattering cross-section is presented in Fig. 5. The contributions from Coulomb scattering and recoiling as well as the s-wave nuclear scattering are positive while the Mott and Coulomb-Nuclear interference terms are negative. It is also notable that above 0.5 MeV the nuclear scattering terms dominate the differential scattering cross section.

To test the validity of the empirical predictor (Eqs. (11)–(18)) the predicted cross-sections were compared with independant high-precision p–p experimental scattering cross-section data [31,32]. This data was not included in the fit (Eq. (18)) and hence represents a valid test of the prediction. Fig. 6 shows the comparison of the empirical prediction after the data had been transformed to the laboratory reference frame. This reference frame was used for the comparison because it is more meaningful for ion beam analysis applications. The transformation for p–p scattering where $M_1 = M_2$ is,

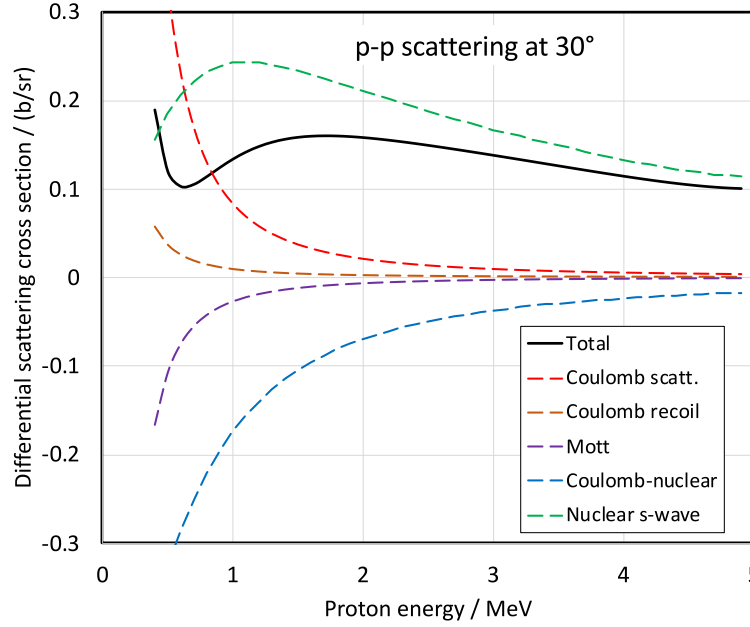$$\theta_l = \theta_c/2, \tag{19}$$

Fig. 5. Contributions from a_0 to a_4 (Eqs. (12)–(16)) and the total p–p scattering cross section in the laboratory reference frame for $\theta_l = 30°$.
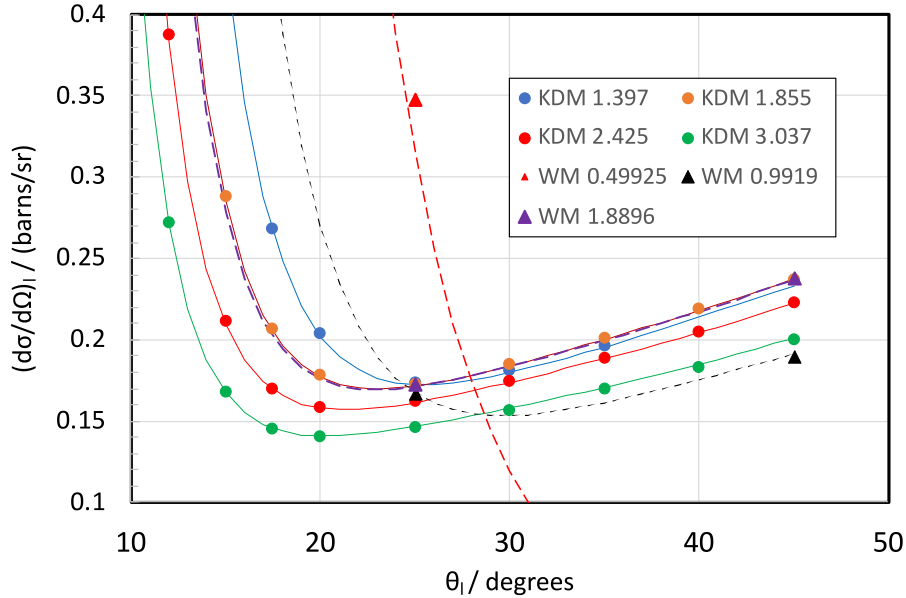

Fig. 6. Angular dependence of the predicted p–p scattering differential cross sections and independant high accuracy experimental data at different proton energies in MeV from Knecht, Dahl and Messelt (KDM) [31] and Wassmer and Mürhy (WM) [32]. The colours correspond to the numerical value of the measurement energies in MeV given in the key. Solid lines and filled circles denote the KDM data. Dashed lines and filled triangles denote the WM data.

and,

$$\left(\frac{d\sigma}{d\Omega}\right)_l = \left[\frac{2}{1+\cos\left(\theta_c/2\right)}\right]^{\frac{1}{2}} \left(\frac{d\sigma}{d\Omega}\right)_c. \tag{20}$$

Clearly the differential cross sections from the predictions of Eqs. (11)–(18) are in extremely close agreement with the high accuracy experimental data of Knecht et al. [31] and Wassmer and Mürhy [32]. For data points in the θ_l range $10° - 45°$ and energy range 0.9 to 3.04 MeV the root mean square relative deviations between the prediction and the literature data is 0.21% for the data of Knecht et al. and 0.56% for the data from Wassmer and Mürhy At 0.5 MeV the relative deviation from the latter data set increased to 6.8%.

Electronic screening, which is not included in the predictions can influence the scattering cross sections. This will be most serious at the lowest proton energy (0.5 MeV) which corresponds to a collision parameter $t^{1/2} = 111$ at a lab angle of 30° [33]. Extrapolating the asymptotic behaviour of Figure 2 of Ref. [34] to our large $t^{1/2}$, implies any effect of screening is at, or below, the 0.1% level. Taken with the agreement between independent experimental data and the predictions in Fig. 6, this implies we may use the empirical predictor with confidence over the angle and energy range of interest for OA-STIM.

4.2. Proton–light element forward scattering cross sections for OA-STIM

For thin samples, the forward-scattered proton signals from light elements (e.g. C, N and O) can be sufficiently well separated to allow
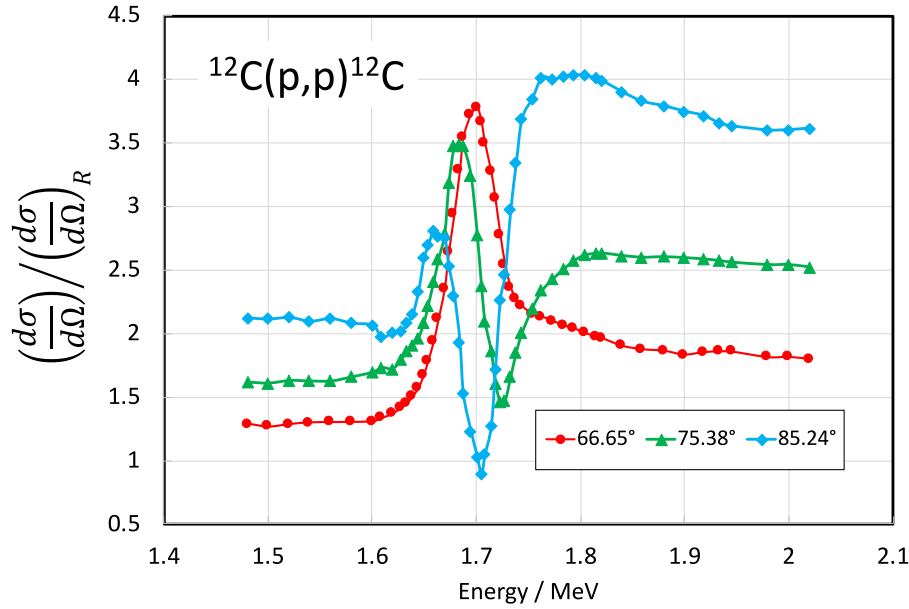
Fig. 7. Energy dependence of the ^{12}C(p,p) ^{12}C elastic scattering cross section normalised to the Rutherford value for large forward scattering angles. The experimental data from [41] was replotted from data retrieved from the IBANDL database [37].

determination of the area under the light element peaks. E.g. Fig 3 (b) of Ref. [35]. This allows direct measurement of the light element composition of thin films without having to invoke stopping forces and their associated uncertainties. The well defined H/C and H/O ratios of many polymers such as Mylar, also allows ratio of the solid angles of the OA-STIM and EBS detectors to be determined. As discussed in the following section (Section 5) this is useful for calibration where OA-STIM is used in conjunction with EBS.

The atomic content ratio of hydrogen to a light element i in a thin sample can be obtained directly from the yields (Y_H and Y_i) of the corresponding peaks in the OA-STIM spectrum as,

$$\frac{n_H}{n_i} = \frac{Y_H}{Y_i}\left(\frac{d\sigma_i}{d\sigma_{p-p}}\right). \tag{21}$$

$(d\sigma_{p-p}/d\Omega)$ can be obtained from the predictor described in Section 4.1. The determination of $(d\sigma_i/d\Omega)$ for other light elements i is confounded compared to p – p scattering because almost no OA-STIM relevant cross section data is available for forward scattering angles where $\theta_l \leq 45°$. In contrast, in the EBS case with $\theta_l = 90° - 180°$, a semi-empirical predictor code SigmaCalc [36] is available and a considerable amount of data from a range of elements for validation of the predictions is readily accessible from Ref. [37]. These EBS cross section values are generally non-Rutherford and exhibit a pronounced resonance structure [38–40]. Gurbich [38] suggests SigmaCalc [36] can be applied in other regions where the underlying models are valid. However, this is only advisable where suitable experimental data for validation is available to support such extensions. The present lack of available data relevant for OA-STIM thus precludes this approach for cross section data.

4.3. An interpolation procedure for p – ^{12}C elastic scattering

Generally, interpolation procedures are more benign, rugged and computationally straightforward than absolute calculation of physical parameters. No scattering cross section data at OA-STIM relevant angles and energies is currently available. Rutherford scattering represents an exactly defined classical limit. A question that then begs an answer is; *can an interpolation procedure be developed to scale the deviation of the cross section from the Rutherford value to smaller scattering angles from the published large forward-angle data?*

For large forward angles, elastic scattering cross section data for the ^{12}C(p, p) ^{12}C at $\theta_l = 65.65°$, 75.38° and 85.25° [41] was retrieved from [37]. Inspection of this data (Fig. 7, taken directly from [37]) showed that, at these large forward angles, (i) the cross sections are generally larger than the Rutherford values, (ii) The cross sections tend to approach the Rutherford values with decreasing θ_l and (iii) there is a pronounced resonance at ~1.74 MeV that changes shape depending on θ_l.

In the classical limit, the Coulomb field presents an insurmountable potential barrier and the scattering cross section is then purely Rutherford (Eqs. (3)–(5)). The classical limit corresponds to where the energy available to penetrate the Coulomb field is insufficient to bring the projectile within a periapsis distance where any interaction with the strong force field is possible. The classical limit corresponds then to low energy projectiles scattered at small scattering angles and at the same time where electronic screening effects [34] are negligible. An important characteristic of the classical limit is that the particle kinematic [12,15] and quantum wave scattering descriptions [28,42] are equivalent.

Comparison of the location of periapsis in the classical limit with the extent of the nuclear potentials field was useful to envisage the situation. The classical perapsis distance ϱ was calculated starting from binary scattering theory [43–46],

$$g(r) = \left[1 - \frac{b^2}{r^2} - \frac{V(r)}{E_r}\right]^{1/2} = 0, \tag{22}$$

where, b is the impact parameter, $V(r)$ is the interaction potential and $E_r = AE/(A+1)$ the relative kinetic energy of the proton and target atom with $A = M_2/M_1$. Putting $r = \varrho$ at the periapsis and for a Coulomb potential,
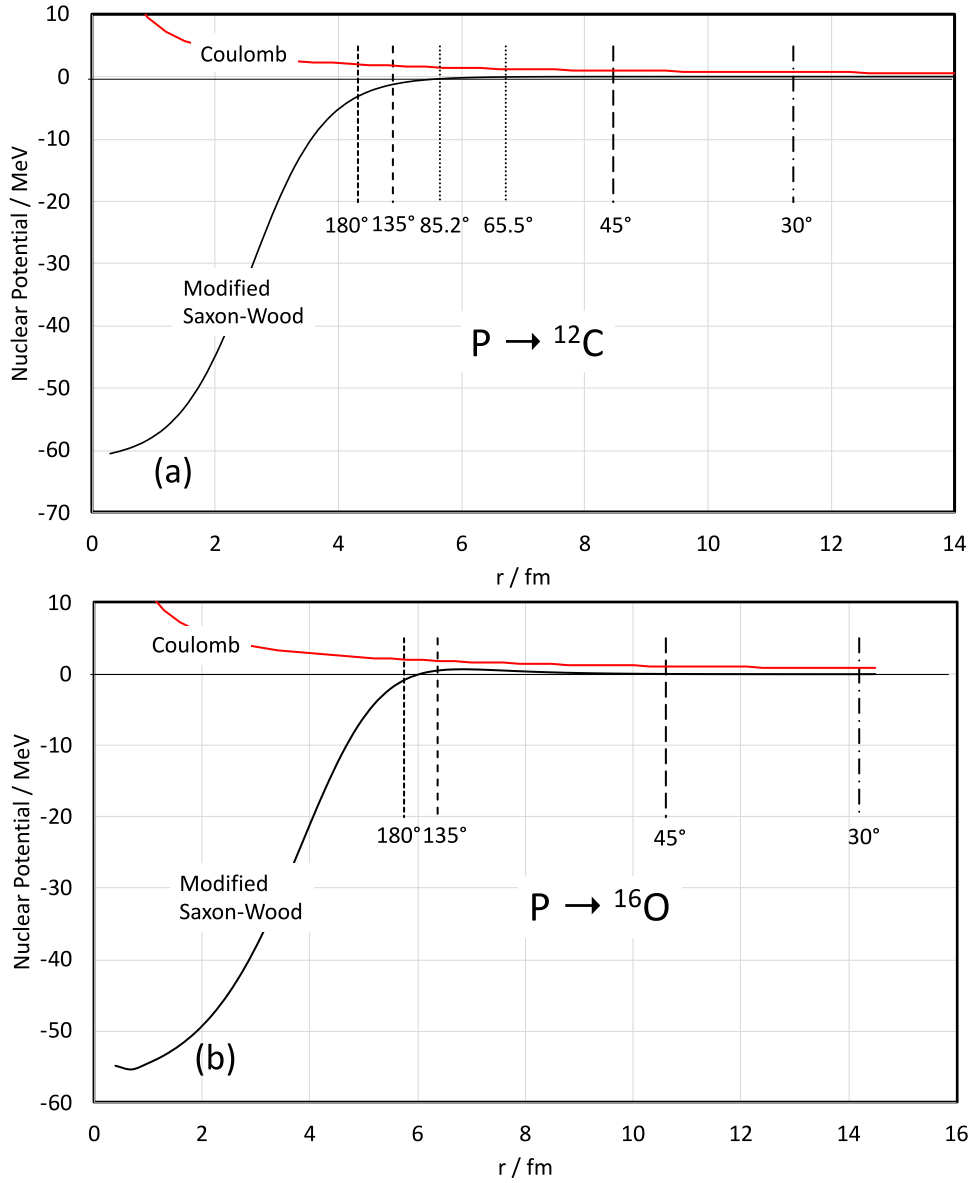
$$V(\varrho) = \frac{\kappa}{\varrho} \text{ with, } \kappa = \frac{Z_1 Z_2 e^2}{4\pi\varepsilon_0}, \tag{23}$$

Eq. (22) can be written as a quadratic equation with only a single physically meaningful positive root. After some manipulation [46] this yields,

$$\varrho = \frac{\kappa}{2E_r} \pm \left(\frac{\kappa^2}{4E_r^2} + b^2\right)^{1/2} = \frac{\kappa}{2E_r}\left[1 + \frac{1}{\sin\theta_c/2}\right], \tag{24}$$

The location of the classical periapsis ϱ for 2 MeV protons was calculated at angles representative for OA-STIM and EBS was calculated

Fig. 8. Modified Saxon-Wood optical-model and Coulomb potentials for (a) p – ^{12}C [38] and (b) p – ^{16}O [40] scattering. The vertical dashed lines indicate the classical periapsis distance (ϱ) for scattering of 2 MeV protons at different scattering angles.

using standard binary scattering theory [43–46]. The classical periapsis corresponding to the large forward angle scattering data for ^{12}C(p,p) ^{12}C elastic scattering of Armstrong et al. [41] was retrieved from [37] was also calculated. Fig. 8 compares ϱ for the different measurement scenarios with the reconstructed nuclear- and Coulomb-potentials for ^{12}C(p,p) ^{12}C and ^{16}O(p, p)^{16}O scattering. The nuclear potentials were a modified Saxon-Woods form using the optical model [47] parameters from Gurbich [38,40]. From Fig. 8 it was observed that for EBS angles the ϱ lay at the edge of the nuclear potential abyss whereas for OA-STIM angles ϱ was 4–8 fm from the edge. Fig. 8(b) showed that for the large forward scattering angles of Ref. [41] ϱ was 1–2 fm outside the edge. Clearly, for the EBS case Fig. 8 supports the suggestion of Gurbich [48] that for EBS the potential barrier is essentially unimportant and the scattering is governed by shape resonances and isobaric analogue state resonances. On the contrary, for forward scattering angles ϱ lies distant from edge from the nuclear potential. For the data of Ref. [41] the non-Rutherford cross sections seen in Fig. 7 gave an important clue that quantum tunnelling should be incorporated in the basis of the interpolation. Taking the scattering cross to be made up of the well-defined

Rutherford contribution and a perturbation contribution.

$$\left(\frac{d\sigma}{d\Omega}\right)_c = \left(\frac{d\sigma_{Ruth}}{d\Omega}\right)_c + \Delta_c, \tag{25}$$

This pointed to the assumption where the perturbation Δ_c of the cross section from the Rutherford value for a given proton energy would be $\Delta_c \propto P^2$. The particle/wave inelastic scattering has identical entrance and exit channels giving a squared dependence on P, the penetration factor.

Fig. 8 indicated that the Gamow factor P_G might represent a suitable scaling law for interpolation. This factor is the transmission factor for quantum tunnelling through an isotropic Coulomb barrier [49–51].

$$P_G = \exp\left(-\sqrt{\frac{E_G}{V_c(\varrho)}}\right), \tag{26}$$

with,

$$E_G = 2M_0c^2\left(\alpha\pi Z_1 Z_2\right)^2 \tag{27}$$

M_0 is the reduced mass in the centre of mass system. A first attempt to scale Δ_c according to this parameter was unsuccessful because the fitted
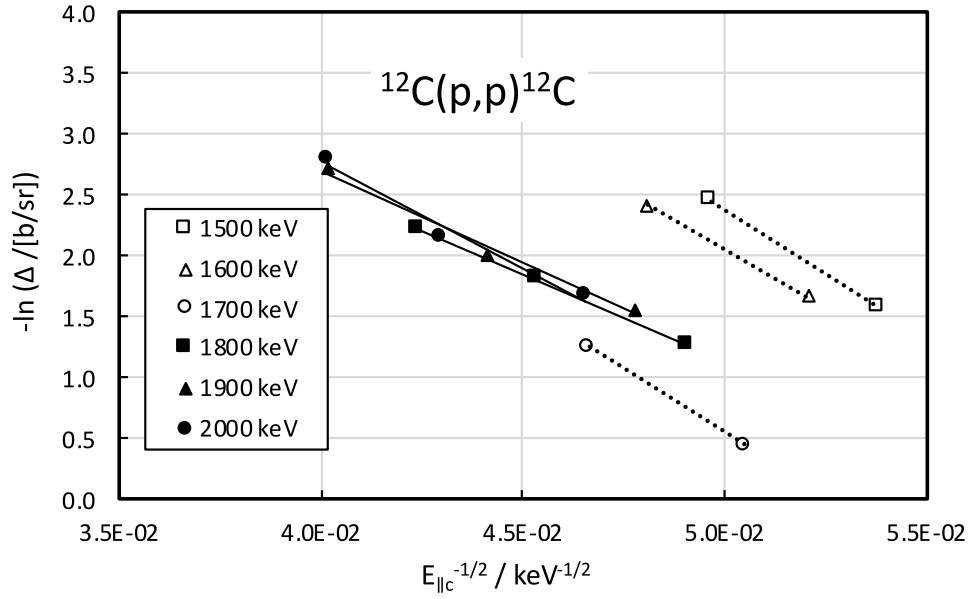
Fig. 9. Plot of the logarithm of the deviation Δ from the Rutherford value for the data Armstrong et al. [41] retrieved from [37] vs. inverse square root of kinetic energy along the collision axis (see text). Some data points were omitted because $\Delta_c < 0$, or a shift in the resonance energy with angle. Solid lines and filled data points denote data sets where three points confirm a straight line dependence. The open data points and dashed lines denote where only two data points were valid. The uncertainties are of the order of the scatter in the data points.

lines from the experimental data points did not pass through the origin as the classical limit was approached. This implied a more sophisticated approach that also takes into partial wave scattering and resonances was necessary.

Iliadis [52] described a penetration factor P_ℓ for scattering of charged particles with arbitrary angular momentum quantum number ℓ where nuclear states give rise to Breit-Wigner like resonances. The full formalism [52] is outside the scope of this work. For the purpose of interpolation, P_ℓ was approximated by,

$$P_\ell \sim \exp\left[-A\,(E)^{-1/2} - B\ell\,(\ell+1)\right], \tag{28}$$

where A and B are constants. A is governed by the Gamow factor while the second term is related to the partial wave scattering factors [53]. For the ^{12}C(p,p) ^{12}C reaction at OA-STIM relevant energies, the penetration is dominated by s-waves $\ell = 0$ with $P_1 \sim 0.1 P_0$ and $P_n > P_{n+1}$ [52]. This facilitated rewriting Eq. (28) in terms of the cross section deviation Δ_c (Eq. (31)),

$$-\ln \Delta_c \sim \frac{C}{\sqrt{E}} + D\ell\,(\ell+1). \tag{29}$$

This represents a straight-line dependence of $\ln \Delta_c$ on $1/\sqrt{E}$ with C and D, constants. Fig. 9 presents such a plot for the experimental data from Ref. [41] at 100 keV intervals from 1.5 to 2.0 MeV. $E_{\parallel c}$ is the kinetic energy associated with the momentum parallel with the collision axis.

The assigned straight lines in Fig. 9 all have similar slopes. The data points for 1.8–2.0 MeV were based on three data points and was fitted well by straight lines. This implied Eq. (29) can be used as the basis of interpolation for these energies. For lower energies (1.5–1.7 MeV) where lines were assigned using only two data points this conclusion must remain tentative until more data becomes available. Since the slopes are constant, the leading term was a Gamow factor. It is then implicit from Eq. (29) that Δ_c goes smoothly to zero as the energy decreases.

From the assigned straight lines of Fig. 9, the fractional deviation from the Rutherford cross section were plotted in Fig. 10 for $\theta_l = 30°$ and $45°$. The uncertainties which originated from the fitting and the experimental data were estimated to be $\sim\pm$ 0.5% where 3 points were used and $\sim\pm$ 0.8 % for 2 points. A caveat is that the experimental cross sections are not so large that Δ_c becomes non-linear. In this case the data in Fig. 10 should be treated as upper limits. This is motivated by a large Δ_c combined with the exponential behaviour of the leading Gamow term. Planely, the $\sim$1.74 MeV resonance influences deviation of the elastic scattering cross section from the Rutherford value. It was evident that the effect of the Gamow term gives a strongly attenuated deviation from the resonance at 30° and 45° compared to the large forward angle experimental data of Fig. 7. The Gamow term also implies a general behaviour that deviations from the Rutherford value will tend to become smaller as the scattering angle decreases.

4.3.1. Extension to other elements than carbon

In spite of an extensive search, no relevant experimental data for forward angles was found for forward scattering of protons from nitrogen and oxygen. Since Z_2 for these elements exceeds that of carbon, the Coulomb field is stronger and consequently the periapsis lies further out from the nuclear field as seen by comparing Fig. 8(a) and (b). This will give a wider and higher potential barrier. The exponential-like dependence of the leading Gamow term in Eq. (28) suggests that the cross sections deviations will be smaller than for the ^{12}C case. However, this conclusion must also remain speculative until more experimental cross section data is available for OA-STIM conditions.

The findings that the deviations from Rutherford scattering are small is supported by the experimental observation that an OA-STIM measurement on Pioloform using Rutherford cross section values at $\theta_l = 45°$ yielded a composition that was in very close agreement with the theoretical composition [35].

5. Simultaneous OA-STIM and EBS

In OA-STIM the light element signals from scattering of light elements are separated from H by having a much greater energy. The OA-STIM signals from elements such as C, N and O quickly become superposed as the sample thickness increases. EBS has the advantage that the larger scattering angle gives a greater separation in backscattering energy compared to OA-STIM according to Eq. (1). In the EBS case for thick samples the heights of the high energy edges h_i, h_j for different elements i, j in the energy spectrum correspond to the surface
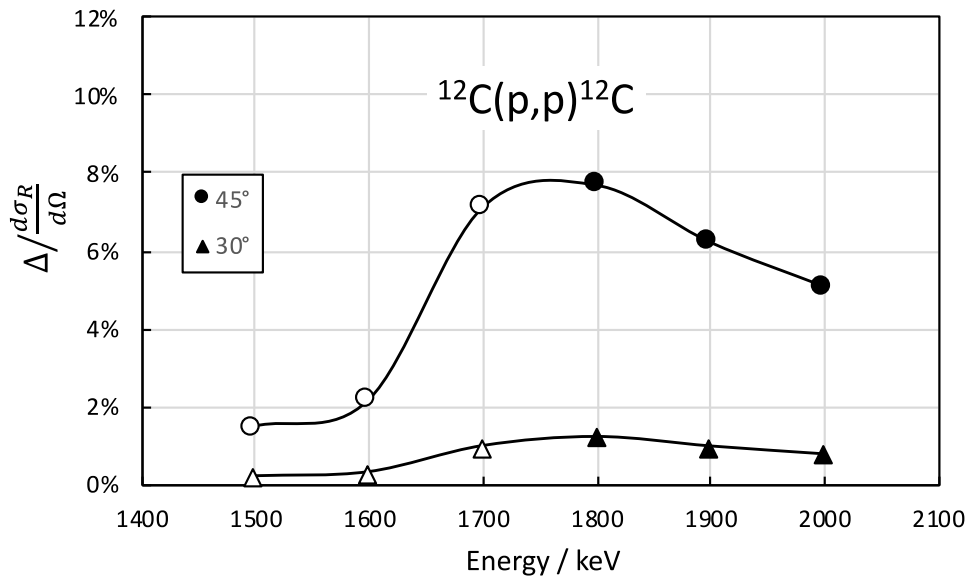
Fig. 10. Relative deviation of the differential scattering cross section $\Delta/\left(d\sigma/d\Omega_R\right)$ vs. laboratory frame Energy. (The relative values are unchanged between both reference frames.) Filled data points denote where the data is based on three experimental data points and open data points where the data is based on only two valid data points.

composition of the sample. Then the relative surface composition for EBS is,

$$\frac{n_i}{n_j} = \frac{h_i}{h_j}\frac{d\sigma_j}{d\sigma_i}\frac{[\epsilon]_j}{[\epsilon]_i}. \tag{30}$$

Generally, the differential scattering cross sections $d\sigma_i/d\Omega$ are non-Rutherford and can be obtained from experimental data or a predictor such as SigmaCalc [36]. $[\epsilon]$ are the usual stopping cross section factors [12,15]. It is straightforward to extend Eq. (30) to determine the hydrogen content from height of the low energy edge of the hydrogen OA-STIM signal by introducing the relative detector solid angles for the OA-STIM and EBS detectors using the predicted p–p scattering cross section (Section 4.2). In OA-STIM measurements of the mean composition over a limited spatial regions of the sample is often of interest. Energy broadening due to thickness variations over the region as well as straggling and multiple scattering may completely confound determination of the low-energy edge height for hydrogen. Since EBS is not a transmission measurement the surface edge heights for other light elements in the EBS spectrum are on the other hand unaffected by thickness variations. Where the hydrogen content is uniform in depth over the spatial region of interest the total yield of hydrogen Y_H is well defined. Then Eq. (30) can be extended to give the relative hydrogen to element j content ratio,

$$\frac{n_H}{n_j} = \frac{Y_H}{h_j}\frac{E_{ch}}{\Delta E_1}\frac{[\epsilon]_H}{[\epsilon]_j}\frac{1}{Y} \tag{31}$$

Here, Y_H is the yield under the hydrogen peak in the OA-STIM spectrum, E_{ch} is the energy channel width in the EBS spectrum and ΔE_i is the energy width in the OA-STIM spectrum corresponding to the sample thickness (Eq. (8)). (A correction can be applied here for the H content of a supporting films.) Y is a factor that relates the signal in the OA-STIM detector to the signal for element i in the EBS detector.

$$Y = \frac{d\sigma_{p-p}}{d\sigma_i}\frac{\Omega_{OA-STIM}}{\Omega_{EBS}}. \tag{32}$$

Y can be measured using a thin reference standard, (such as a polymer film) with e.g. a known n_H/n_i atomic ratio as in the case of PESA. An alternative approach, to determine Y which is restricted to thin reference standards is to use the p–p scattering cross section from Section 4.1 with the detector solid angle ratio $\Omega_{OA-STIM}/\Omega_{EBS}$ determined from scattered proton yield ratio for element i in the OA-STIM and EBS

detectors. The second method has the advantage that it is based on the direct measurement of the relative yields of the same element in both detectors. This ratio will be unaffected by proton bombardment induced composition changes in the reference film. An example of such composition changes can be seen in Ref. [35].

It follows that using the above approach, the light element composition (including hydrogen) and thickness of regions of thin films such as biological tissue sections e.g. [11] can be quantified using simultaneous EBS and OA-STIM. There is no fundamental reason why this approach cannot be extended to samples comprising two or even multiple homogeneous films of hydrogenous materials.

6. Conclusions

A formalism for quantitative off-axis Scanning Transmission Ion Microscopy OA-STIM) has been developed.

- The transmission geometry for OA-STIM implies the highest energy scattered protons originate from the rear-face of the sample and the energies corresponding front and rear surfaces depend on thickness variations in the sample.
- The proton–proton (p–p) scattering cross section is contributed to by Rutherford scattering and recoils as well as nuclear scattering, Mott scattering and Coulomb-nuclear interference terms. An empirical predictor for $d\sigma_{p-p}/d\Omega$) was established. This based on one free parameter (the nuclear phase shift) and the predictions were in very close agreement with independent high accuracy literature data (0.6%) over the energy and angle region used in OA-STIM measurements.
- A non-linear interpolation method based on penetration of the nuclear potential barrier has been established for ^{12}C(p,p)^{12}C elastic scattering. This predicts that for OA-STIM with 2 MeV protons an upper limit for the deviation of the cross section from Rutherford value to be ≤6.4% for scattering at ≤45°.
- Using simultaneous OA-STIM and EBS can be used to measure the composition including H of thin films over a region, even where significant thickness variations are present.

CRediT authorship contribution statement

Harry J. Whitlow: All development of the formalism, All collection and analysis of literature data, Prepared figures, Writing – original draft.

Declaration of competing interest

Data availability

Data will be made available on request.

Acknowledgements

References

[1] M.B.H. Breese, D.N. Jamieson, P.J.C. King, Materials Analysis using a Nuclear Microprobe, John Wiley and Sons Inc., New York, 1996, pp. 173–183.

[2] R. Minqin, J. van Kan, A. Bettiol, L. Daina, C.Y. Gek, B.B. Huat, H. Whitlow, T. Osipowicz, F. Watt, Nano-imaging of single cells using STIM, Nucl. Instrum. Methods Phys. Res. B 260 (1) (2007) 124–129, http://dx.doi.org/10.1016/j.nimb.2007.02.015, URL https://www.sciencedirect.com/science/article/pii/S0168583X07003539, Nuclear Microprobe Technology and Applications (ICNMTA2006) and Proton Beam Writing (PBW II).

[3] R. Norarat, V. Marjomäki, X. Chen, M. Zhaohong, R. Minqin, C.-B. Chen, A. Bettiol, H. Whitlow, F. Watt, Ion-induced fluorescence imaging of endosomes, Nucl. Instrum. Methods Phys. Res. B 306 (2013) 113–116, http://dx.doi.org/10.1016/j.nimb.2012.12.052, URL https://www.sciencedirect.com/science/article/pii/S0168583X13000281, 13th International Conference on Microprobe Technology and Applications (ICNMTA2012).

[4] H. Hofsäss, Coincidence Techniques, Springer US, Boston, MA, 1996, pp. 209–245, http://dx.doi.org/10.1007/978-1-4613-0353-4_9.

[5] G. Bench, P.G. Grant, D. Ueda, S.S. Cliff, K.D. Perry, T.A. Cahill, The use of STIM and PESA to measure profiles of aerosol mass and hydrogen content, respectively, across mylar rotating drums impactor samples, Aerosol Sci. Technol. 36 (5) (2002) 642–651, http://dx.doi.org/10.1080/02786820252883874, arXiv:http://dx.doi.org/10.1080/02786820252883874.

[6] M. Chiari, G. Calzolai, M. Giannoni, F. Lucarelli, S. Nava, S. Becagli, Use of proton elastic scattering techniques to determine carbonaceous fractions in atmospheric aerosols collected on teflon filters, J. Aerosol Sci. 89 (2015) 85–95, http://dx.doi.org/10.1016/j.jaerosci.2015.07.006, URL https://www.sciencedirect.com/science/article/pii/S0021850215001123.

[7] J. Voltr, J. Král, Z. k Nejedlý, PESA as a complementary tool to PIXE at CTU prague, Nucl. Instrum. Methods Phys. Res. B 150 (1) (1999) 554–558, http://dx.doi.org/10.1016/S0168-583X(98)00951-3, URL https://www.sciencedirect.com/science/article/pii/S0168583X98009513.

[8] E.N. Marieb, Human Anatomy & Physiology, 6th, Pearson Benjamin Cummings, 2004.

[9] P.A. Hasgall, F.D. Gennaro, B.L. C. Baumgartner andE. Neufeld, M.C. Gosselin, D. Payne, A. Klingenböck, N. Kuster, It'is database for thermal and electromagnetic parameters of biological tissues, 2022, URL DOI:10.13099/VIP21000-04-1.itis.swiss/database.

[10] G.R. Rossman, Hydrogen in "anhydrous" minerals, Nucl. Instrum. Methods Phys. Res. B 45 (1) (1990) 41–44, http://dx.doi.org/10.1016/0168-583X(90)90780-X, URL https://www.sciencedirect.com/science/article/pii/0168583X9090780X.

[11] H.J. Whitlow, G. Nagy, N. Henderson, R. Greco, N. Deoli, K.M. Smith, K. Morgan, F. Villinger, Sequestration of Ca in simian nasal mucosa: determination of Ca molarities in live tissue by simultaneous off-axis scanning transmission ion microscopy, particle induced X-ray emission and rutherford backscattering spectrometry, Nucl. Instrum. Methods B 539 (2022) 152–161, http://dx.doi.org/10.1016/j.nimb.2023.03.029, URL https://www.sciencedirect.com/science/article/pii/S0168583X23001179.

[12] W.-K. Chu, J.W. Mayer, M.-A. Nicolet, Backscattering Spectrometry, Academic Press, New-York, 1978.

[13] K.S. Krane, Introductory Nuclear Physics, John Wiley and Sons, New-York, 1988, pp. 818–821.

[14] J.F. Ziegler, R. Lever, Calculation of elastic scattering of ⁴He projectiles for m thin layers, Thin Solid Films 19 (1973) 291–296.

[15] M. Nastasi, J.W. Mayer, Y. Wang (Eds.), Ion Beam Analysis: fuandamentals and applications, CRC Press,Taylor & Francis Group, Boca Raton FL, 33487, USA, 2015, pp. 79–110.

[16] H. Whitlow, G. Possnert, C.S. Petersson, Quantitative mass and energy dispersive elastic recoil spectrometry: resolution and efficiency considerations, Nucl. Instrum. Methods B 27 (1987) 448, http://dx.doi.org/10.1016/0168-583X(87)90527-1, URL https://www.sciencedirect.com/science/article/abs/pii/0168583X87905271.

[17] P. Sigmund, A. Schinner, Binary theory of electronic stopping, Nucl. Instrum. Methods Phys. Res. B 195 (1) (2002) 64–90, http://dx.doi.org/10.1016/S0168-583X(01)01162-4, URL https://www.sciencedirect.com/science/article/pii/S0168583X01011624.

[18] A. Schinner, P. Sigmund, Expanded PASS stopping code, Nucl. Instrum. Methods Phys. Res. B 460 (2019) 19–26, http://dx.doi.org/10.1016/j.nimb.2018.10.047, URL https://www.sciencedirect.com/science/article/pii/S0168583X18306396, Special Issue: SHIM-ICACS Swift Heavy Ions in Matter and International Conference on Atomic Collisions in Solids, 1-7 July 2018 Caen, France.

[19] J.F. Ziegler, M. Ziegler, J. Biersack, SRIM – The stopping and range of ions in matter (2010), Nucl. Instrum. Methods Phys. Res. B 268 (11) (2010) 1818–1823, http://dx.doi.org/10.1016/j.nimb.2010.02.091, URL https://www.sciencedirect.com/science/article/pii/S0168583X10001862, 19th International Conference on Ion Beam Analysis.

[20] D.I. Thwaites, Bragg's rule of stopping power additivity: A compilation and summary of results, Radiat. Res. 95 (3) (1983) 495–518, http://dx.doi.org/10.2307/3576096.

[21] H. Whitlow, M. Ren, X. Chen, T. Osipowicz, J.A. van Kan, F. Watt, PESA angular spreading measurements using Mev ions microscopes, Nucl. Instrum. Methods Phys. Res. B 306 (2013) 311, http://dx.doi.org/10.1016/j.nimb.2012.11.035.

[22] J.D. Jackson, J.M. Blatt, The interpretation of low energy proton-proton scattering, Rev. Modern Phys. 22 (1950) 77–118, http://dx.doi.org/10.1103/RevModPhys.22.77, URL https://link.aps.org/doi/10.1103/RevModPhys.22.77.

[23] D.E.F. H. R. Worthington, Proton-proton scattering from 1.8 to 4.2 MeV, Phys. Rev. 90 (1953) 899–911.

[24] H. Hall, J. Powell, Scattering of protons by protons, Phys. Rev. 90 (1953) 912–914.

[25] R.D. Evans, The atomic nuclius, Tata McGraw-Hill, Bombay, 1955, pp. 338–344.

[26] N. Mott, The collison between two electrons, Proc. R. Soc. A 126 (1930) 259–267, URL https://doi.org/10.1098/rspa.1930.0006.

[27] K. Krane, Introductory Nuclear Physics, John Wiley and Sons, New-York, 1988, pp. 97–100.

[28] C.J. Joachain, Quantum Collision Theory, North Holland, Amsterdam, 1975, pp. 156–159.

[29] A. Peres, Low-energy proton-proton scattering, Nuclear Phys. A 312 (3) (1978) 291–296, http://dx.doi.org/10.1016/0375-9474(78)90591-2, URL https://www.sciencedirect.com/science/article/pii/0375947478905912.

[30] L.L. Foldy, E. Eriksen, Vacuum polarization and proton-proton scattering, Phys. Rev. 98 (1955) 775–779, http://dx.doi.org/10.1103/PhysRev.98.775, URL https://link.aps.org/doi/10.1103/PhysRev.98.775.

[31] D.J. Knecht, P.F. Dahl, S. Messelt, Proton-proton scattering: Revision and analysis of experimental measurements from 1.4 to 3.0 MeV, Phys. Rev. 148 (1966) 1031–1044, http://dx.doi.org/10.1103/PhysRev.148.1031, URL https://link.aps.org/doi/10.1103/PhysRev.148.1031.

[32] H. Wassmer, H. Mürhy, Proton-proton streuung im energieberich von 500 - 2000 kev: Resultate und auswertung, Helv. Phys. Acta 46 (1973) 626–634.

[33] J. Lindhard, V. Nielsen, M. Scharff, Approximation method in classical scattering by screened Coulomb fields (notes on atomic collsions i), Det Kgl. Dan. Vidensk. Selsk., Mat.-Fys. Medd. 36 (10) (1968) 1–32.

[34] H.H. Andersen, F. Besenbacher, P. Loftager, W. Möller, Large-angle scattering of light ions in the weakly screened rutherford region, Phys. Rev. A 21 (1980) 1891–1901, http://dx.doi.org/10.1103/PhysRevA.21.1891, URL https://link.aps.org/doi/10.1103/PhysRevA.21.1891.

[35] H.J. Whitlow, G. Nagy, Proton beam induced degradation of pioloform® (polyvinyl butyral (PVB)) support films used for analysis of biomedical tissue sections, Nucl. Instrum. Methods B 539 (2022) 136–140, http://dx.doi.org/10.1016/j.nimb.2023.03.028, URL https://www.sciencedirect.com/science/article/pii/S0168583X23001167.

[36] A. Gurbich, SigmaCalc recent development and present status of the evaluated cross-sections for IBA, Nucl. Instrum. Methods Phys. Res. B 371 (2016) 27–32, http://dx.doi.org/10.1016/j.nimb.2015.09.035, URL https://www.sciencedirect.com/science/article/pii/S0168583X15008940, The 22nd International Conference on Ion Beam Analysis (IBA 2015).

[37] A. Gurbich, Ion beam analysis nuclear data libary, 2019, URL https://www-nds.iaea.org/exfor/ibandl.htm.

[38] A. Gurbich, Evaluation of non-rutherford proton elastic scattering cross section for carbon, Nucl. Instrum. Methods Phys. Res. B 136–138 (1998) 60–65, http://dx.doi.org/10.1016/S0168-583X(97)00837-9, URL https://www.sciencedirect.com/science/article/pii/S0168583X97008379, Ion Beam Analysis.

[39] A. Gurbich, Evaluation of non-rutherford proton elastic scattering cross section for nitrogen, Nucl. Instrum. Methods Phys. Res. B 266 (8) (2008) 1193–1197, http://dx.doi.org/10.1016/j.nimb.2007.11.026, URL https://www.sciencedirect.com/science/article/pii/S0168583X07017235, Ion Beam Analysis.

[40] A. Gurbich, Evaluation of non-rutherford proton elastic scattering cross section for oxygen, Nucl. Instrum. Methods Phys. Res. B 129 (3) (1997) 311–316, http://dx.doi.org/10.1016/S0168-583X(97)00288-7, URL https://www.sciencedirect.com/science/article/pii/S0168583X97002887.

[41] J.C. Armstrong, M.J. Baggett, W.R. Harris, V.A. Latorre, 1.7-MeV anomaly in the $c^{12}(p, p)c^{12}$ reaction, Phys. Rev. 144 (1966) 823–828, http://dx.doi.org/10.1103/PhysRev.144.823, URL https://link.aps.org/doi/10.1103/PhysRev.144.823.

[42] E. Mertzbacher, Quantum Mechanics, second ed., John Wiley and Sons, New York, 1970, pp. 240–250.

[43] M.W. Thompson, Defects and Radiation Damage in Metals, Cambridge Unviersity Press, London, 1969, pp. 105–107.

[44] M.T. Robinson, Sputtering by Particle Bombardment I, in: Topics in Appleid Physics, 47, Springer Verlag, 1981, pp. 96–97.

[45] P. Sigmund, Elastic scattering, in: Particle Penetration and Radiation Effects: General Aspects and Stopping of Swift Point Charges, Springer Berlin Heidelberg, Berlin, Heidelberg, 2006, pp. 67–105, http://dx.doi.org/10.1007/3-540-31718-X_3.

[46] H. Herget, Classical mechanics worksheet 8, 2021, URL https://people.nscl.msu.edu/~hergert/phy820/material/pdfs/w08.pdf.

[47] K.S. Krane, Introductory Nuclear Physics, John Wiley and Sons, New-York, 1988, pp. 413–416.

[48] A. Gurbich, On the concept of an actual Coulomb barrier, Nucl. Instrum. Methods Phys. Res. B 217 (1) (2004) 183–186, http://dx.doi.org/10.1016/j.nimb.2003.12.043, URL https://www.sciencedirect.com/science/article/pii/S0168583X03022675.

[49] G. Gamow, Zur quantentheorie des atomkernes, Z. Phys. 51 (3) (1928) 204–212, http://dx.doi.org/10.1007/BF01343196.

[50] G. Gamow, The quantum theory of nuclear disintegration, Nature 122 (3082) (1928) 805–806, http://dx.doi.org/10.1038/122805b0.

[51] K.S. Krane, Introductory Nuclear Physics, John Wiley and Sons, New-York, 1988, p. 253,773.

[52] C. Iliadis, Nuclear Physics of Stars, second ed., Wiley VCH, Weinheim, Germany, 2015, p. 112,116.

[53] K.S. Krane, Introductory Nuclear Physics, John Wiley and Sons, New-York, 1988, pp. 400–413.